Electronic Supplementary Material (ESI)

1. General methods

Materials and reagents

The fresh bovine blood was purchased from slaughter house in Beijing. Hydrochloric acid (HCl), acetic acid, ethanol, methanol and sodium chloride (NaCl) were purchased from Sinopharm. Zinc chloride ($ZnCl_2$) and dimethyl formamide (DMF) were purchased from Macklin and Aladdin, respectively. High purity argon, oxygen and nitrogen gas were bought from Beijing AP BAIF Gases Industry Co. Ltd. Commercial Pt/C (20 wt.%), Nafion solution (5 wt.%) were purchased from Alfa Aesar and DuPont, respectively. Ultrapure water (18.2 MΩ cm) obtained from a water purification system (TTL-6B) without further purity.

Experimental Section

Synthesis of CPC and *non*-PC. For comparison, an identical procedure for the preparation of HPC was conducted only without adding of NaOH, and the resulting carbon material was denoted as CPC (closed-pore structured carbon); a carbon material prepared by direct pyrolysis of serum albumin followed by washing with 2 M HCl, rinsing with distilled water, and dried at 80 °C was denoted as *non*-PC (none porous carbon).

Synthesis of Fe–N–CPC, Fe–N–*non*PC and Fe–N–BC. For comparison, an identical procedure for the preparation of Fe-N-HPC only replacing HPC with CPC or *non*-PC was conducted, and the resulting sample was denoted as Fe–N–CPC or Fe–N–*non*PC. To prove the necessity for the separation and respectively dispose of serum albumin

and red blood cells from bovine blood, another reference sample denoted as Fe–N–BC is synthesized as follows: The fresh bovine blood was dried at 80 °C for 24 h to remove the water within the blood. 6.25 g of the as-prepared powder was dissolved into 67 mL of deionized water, denoted as solution A. 9.38 g of $ZnCl_2$ was dispersed in 67 mL deionized water, denoted as solution B. Then, solution B was added dropwise into solution A and the mixture was vigorously stirred at 60 °C for 10 min. After that, 12 mL of 5 M NaOH was added dropwise and the mixture was kept vigorously stirring for 30 min. Then the mixture was allowed to be filtrated to remove excess NaOH and dried at 80 °C for 24 h. The as-prepared sample was carbonized/activated at 800 °C for 2 h under Ar atmosphere with ramping rate of 2.5 °C min^{-1}. After cooling to room temperature, the obtained product was washed with 2 M HCl, rinsed with distilled water, and dried at 80 °C. then the sample was further pyrolyzed with ramping rate of 5 °C min^{-1} to 900 °C, holding for 3 h, with 2 h under Ar atmosphere and 1 h under NH_3 atmosphere. After cooling to room temperature, the obtained product was washed with 2 M HCl, rinsed with distilled water, and dried at 80 °C, generating the Fe–N–BC.

Material Characterization

Field emission scanning electron microscopy (FE-SEM, JSM-6701, JEOL), transmission electron microscopy (TEM, JSM-2100, JEOL), and high-angle annular dark-field scanning transmission electron microscopy (HAADF-STEM, JEM-ARM200F, JEOL) were used to characterize the morphologies of the samples. The powder X-ray diffraction (XRD) measurement from 10 degree to 90 degree was carried out on a Rigaku D/max-2500 diffractometer equipped with Cu K_α source radiation at

30 KV and 40 mA. The nitrogen adsorption-desorption isotherms were obtained on a Quantachrome AUTOSORB-SI instrument, where the specific surface areas and pore size distribution of the samples were measured by the Brunauer-Emmett-Teller (BET) and density functional theory (DFT) methods, respectively. Raman spectra were profiled with a Horiba Jobin Yvon LabRam HR800 confocal microscope with a visible laser (λ=532 nm) at room temperature. X-ray photoelectron spectroscopy (XPS) (Thermo Fisher Scientific ESCALAB 250) was performed to determine the surface element composition and chemical states of the samples. X-ray absorption fine structure (XAFS) spectra were carried out on the beamline 1W1B station of Beijing Synchrotron Radiation Facility. The Fe K-edge X-ray absorption near-edge structure (XANES) spectra were recorded in a fluorescence mode with Fe foil as reference, and the acquired Fe K-edge extended X-ray absorption fine structure (EXAFS) data were extracted and processed according to standard procedures using ATHENA module implemented in the IFEFFIT software packages. Thermogravimetric analysis (TG, NETZSCH ×70) was carried out with a ramping rate of 10 °C min^{-1} under Ar or air atmosphere. ^{57}Fe Mössbauer spectroscopy measurement was conducted at room temperature using a Topologic 500 A spectrometer with a proportional counter and a radioactive source (moving ^{57}Co (Rh) in a constant acceleration mode). All spectral analyses were conducted assuming a Lorentzian lineshape for computer folding and fitting.

Electrochemical measurement

The electrochemical performance of the electrocatalysts were evaluated using an ALS/DY2300 workstation equipped with three-electrode system at room temperature.

Electrocatalysts coated rotating ring-disk electrode (RRDE) was used as the working electrode, a saturated calomel electrode (SCE) and a Pt wire as the reference and counter electrodes, respectively. All potentials in this work were calibrated with respect to reversible hydrogen electrode (RHE). To prepare the working electrode, the RRDE was firstly polished with a sequence of 1.0, 0.5 and 0.05 μm alumina suspension to afford a mirror surface. Then, 10 μL of homogenous electrocatalyst ink prepared by ultrasonic dispersing electrocatalysts (5 mg) with ethanol (1.0 mL) and 5 wt.% Nafion solution (10 μL) for 0.5 h, was pipetted onto the glassy carbon electrode (GCE, 0.1256 cm^2) to give the electrocatalyst loading of 380 μg_{cat} cm^{-2}. The commercial Pt/C electrode was also prepared in the similar procedure for comparison with a Pt loading of 76 μg_{pt} cm^{-2}.

For the ORR test, the electrocatalyst was first activated by potential cycling between 0 to 1.3 V for 20 cycles with a scan rate of 100 mV s^{-1} in N_2-saturated 0.1 M KOH solution. The LSV curve was corrected by subtracting the LSV curve conducted in N_2-saturated 0.1 M KOH to eliminating the influence of non-Faradaic current (capacitive current). Methanol tolerance capability was evaluated by measuring the LSV curves in O_2-saturated 0.1 M KOH with or without addition of 1 M methanol. The electrochemical stability was evaluated by potential cycling in the range of 0.6 and 1.1 V in O_2-saturated 0.1 M KOH for 3000 cycles (scan rate: 100 mV s^{-1}). The Koutecky–Levich (K-L) plots were profiled according to:

$$J^{-1} = J_k^{-1} + \left(0.2nFC_{O_2}D_{O_2}^{2/3}\gamma^{-1/6}\right)^{-1}\omega^{-1/2} \quad (1)$$

where J is the Faradaic current collected at the glass carbon disk, J_k is the kinetic current, n is the electron transferred number per oxygen molecule, F is the Faraday constant, C_{O_2}, D_{O_2} and γ are the concentration, diffusion coefficient of oxygen and kinematic viscosity, respectively.

For the evaluation of hydrogen peroxide (HO_2^-) yield and four-electron selectivity, the potential of Pt ring was fixed at 1.5 V with electrode rotating rate of 1600 rpm. The yield of HO_2^- and corresponding electron transfer number (n) were calculated according to:

$$\%HO_2^- = 200 \times \frac{I_r/N}{I_d + I_r/N} \quad (2)$$

$$n = 4 \times \frac{I_d}{I_d + I_r/N} \quad (3)$$

where I_d is disk current, I_r is ring current and N is the collection efficiency of Pt ring (N= 0.4) .

2. Characterization

Table S1. BET surface area, surface area of micropore (S_{micro}), surface area of mesopore (S_{meso}), total pore volume, volume of micropore (V_{micro}) and volume of mesopore (V_{meso}) of HPC, HM-adsorbed HPC and Fe-N-HPC.

Sample	S_{BET} ($m^2\ g^{-1}$)	S_{micro} ($m^2\ g^{-1}$)	S_{meso} ($m^2\ g^{-1}$)	% of S_{micro}	% of S_{meso}	Volume ($cm^3\ g^{-1}$)	V_{micro} ($cm^3\ g^{-1}$)	V_{meso} ($cm^3\ g^{-1}$)	% of V_{micro}	% of V_{meso}
non-PC	11.1	0.2	10.9	1.8	98.2	0.01	0	0.01	0	100
CPC	1046.8	917.2	129.6	87.6	12.4	0.49	0.38	0.11	77.6	22.4
HPC	1455.5	1302.6	152.9	89.5	10.5	0.75	0.52	0.23	69.3	30.7

Table S2. Elemental compositions of *non*-PC, CPC, HPC and Fe-N-HPC determined by XPS

Sample	Surface element (XPS)			
	C (at.%)	N (at.%)	O (at.%)	Fe (at.%)
non-PC	72.4	3.4	24.2	–
CPC	80.3	10.0	9.7	–
HPC	81.7	12.2	6.1	–
Fe-N-HPC	82.3	3	14.6	0.1
Sample	**Functionality (% of total N 1s)**			
	Pyridinic N	**Pyrrolic N**	**Graphitic N**	**Oxidized N**
non-PC	42.6	57.4	–	–
CPC	23.3	44.7	23.7	8.3
HPC	26.3	40.9	23.6	9.2
Fe-N-HPC	22.6	29.8	30.3	17.3
Sample	**Functionality (% of total C 1s)**			
	C=C	**C-N**	**COOH**	**Ads CO_2**
non-PC	71.6	10.5	14.4	3.5
CPC	50.2	25.8	17.8	6.2
HPC	46.4	25.6	17.0	11.0
Fe-N-HPC	40.8	45.7	13.5	–

Table S3. The fitting parameters based on the EIS of non-PC, CPC, HPC-700, HPC-800 and HPC-900.

Sample	R_Ω	R_{ct}	R_d
non-PC	7.0	242.5	58
CPC	7.9	6.8	45.5
HPC-700	6.8	1.2	9.0
HPC-800	6.6	3.8	3.0
HPC-900	7.3	4.3	19.5

Table S4. BET surface area, surface area of micropore (S_{micro}), surface area of mesopore (S_{meso}), total pore volume, volume of micropore (V_{micro}) and volume of mesopore (V_{meso}) of HPC, HM-adsorbed HPC and Fe-N-HPC.

Sample	S_{BET} ($m^2\ g^{-1}$)	S_{micro} ($m^2\ g^{-1}$)	S_{meso} ($m^2\ g^{-1}$)	% of S_{micro}	% of S_{meso}	Volume ($cm^3\ g^{-1}$)	V_{micro} ($cm^3\ g^{-1}$)	V_{meso} ($cm^3\ g^{-1}$)	% of V_{micro}	% of V_{meso}
HPC	1455.5	1302.6	152.9	89.5	10.5	0.75	0.52	0.23	69.3	30.7
HM-HPC	1228.4	1078.6	149.8	87.8	12.2	0.6	0.43	0.17	71.7	28.3
Fe-N-HPC	2559.1	2145.9	413.2	83.8	16.2	1.4	0.91	0.49	65	35

Table S5. The relative area for Raman deconvolution.

Sample	*I-line*	*D-line*	*D''-line*	*G-line*
non-PC	9.1%	55.4%	18.0%	17.5%
CPC	11.8%	54.4%	16.5%	17.3%
HPC	11.4%	50.2%	19.2%	19.2%
Fe-N-HPC	6.4%	63.4%	5.6%	24.5%

Table S6. Summary of ORR performance in alkaline electrolyte for recently reported non-precious metal electrocatalysts in the literatures.

Electrocatalyst	**Electrolyte**	$E_{1/2}$ **(V)**	**n**	**Ref.**
Fe@N-C-700	0.1 M KOH	0.83	3.94	[1]
Fe−N−CC	0.1 M KOH	0.83	3.7	[2]
S,N-Fe/N/C-CNT	0.1 M KOH	0.85	4.0	[3]
PPCNS	0.1 M KOH	0.84	3.9	[4]
Fe-N/C	0.1 M KOH	0.848	3.9	[5]
PPy/FeTCPP/Co	0.1 M KOH	0.86	3.9	[6]
Fe2-Z8-C	0.1 M KOH	0.871	3.97	[7]
Fe-NMCSs	0.1 M KOH	0.86	4.0	[8]
CPM-99Fe/C	0.1 M KOH	0.802	-	[9]
Fe-N-HPC	**0.1 M KOH**	**0.87**	**>3.95**	This work

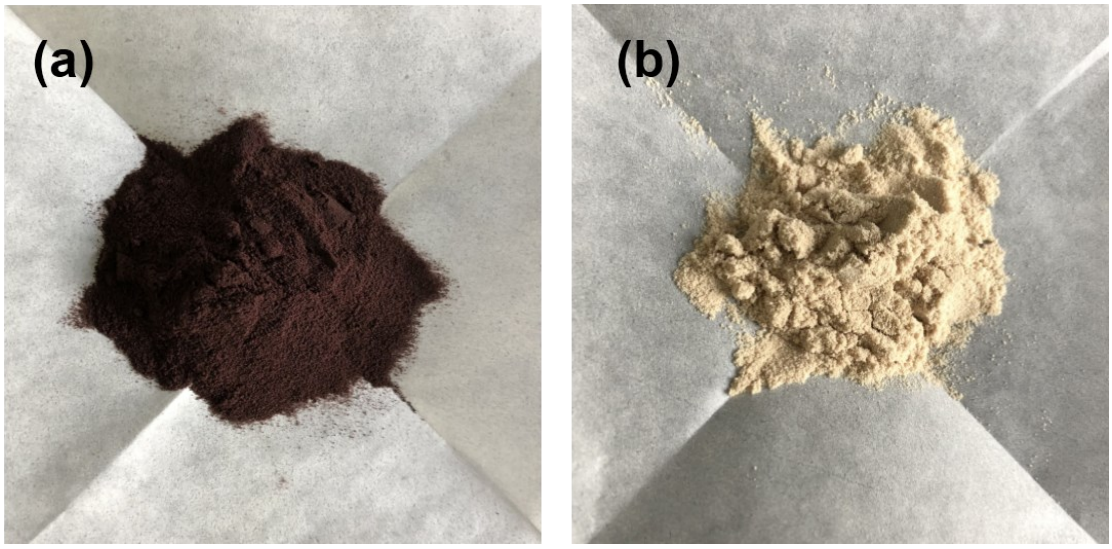

Figure S1. Digital photographs of (a) red blood cells and (b) BSA powder derived from the bovine blood.

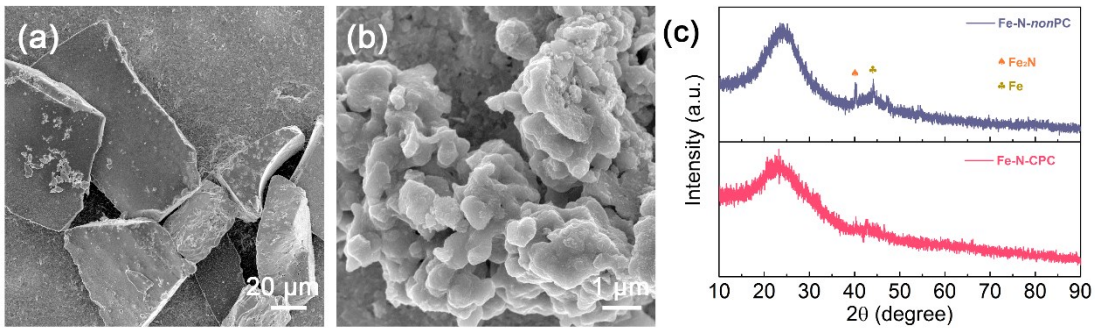

Figure S2. Typical SEM images of (a) *non*-PC and (b) CPC. XRD pattern of Fe-N-*non*PC and Fe-N-CPC.

Thers are no clear macropores and mesopores for *non*-PC and CPC from the SEM observation. After the adsorption and pyrolysis with HM, Fe_2N and Fe evolved for both Fe-N-*non*PC and Fe-N-CPC, which may reasoned by insufficient pores to disperse and anchor the Fe-based single-atom active sites.

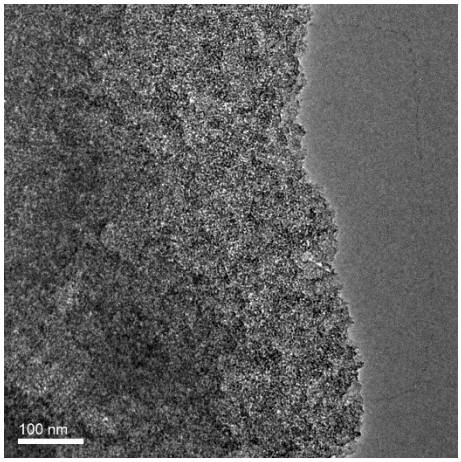

Figure S3. Typical TEM image of CPC.

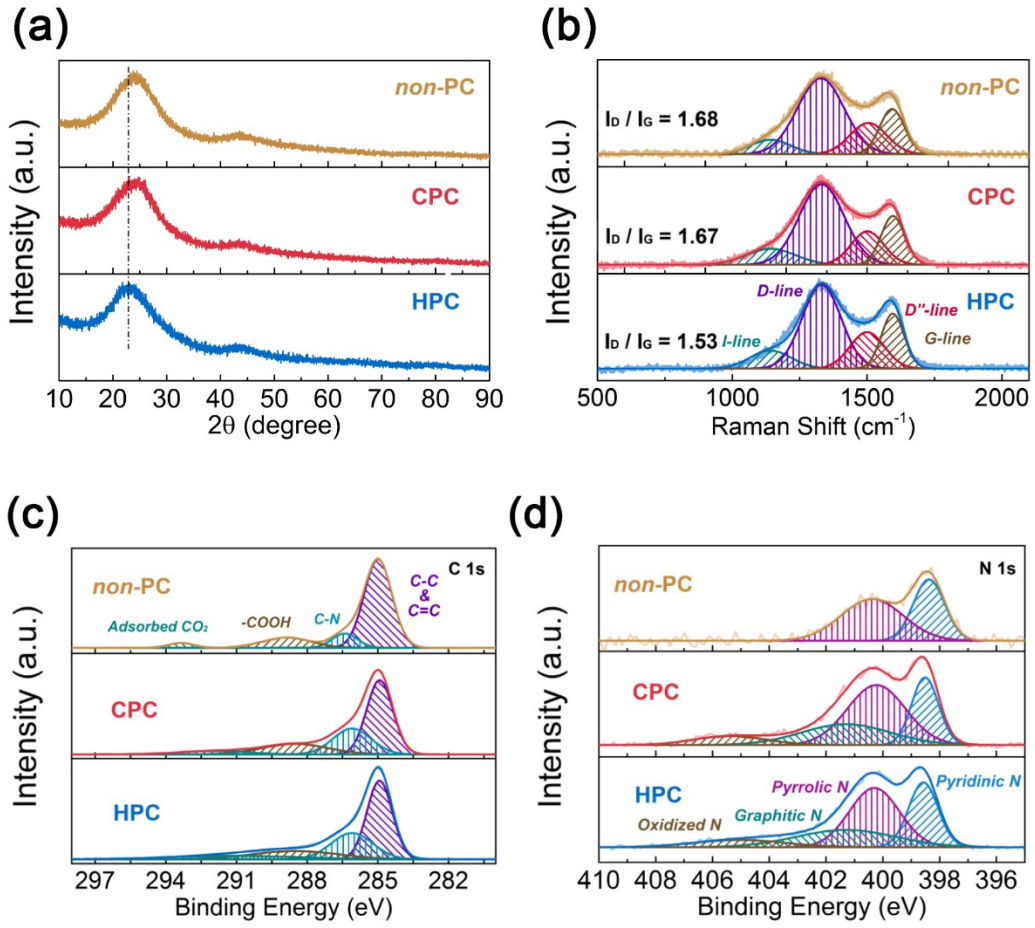

Figure S4. (a) XRD patterns and (b) Raman spectra of *non*-PC, CPC and HPC. High-resolution XPS spectra of (c) C 1s and (d) N 1s for *non*-PC, CPC and HPC.

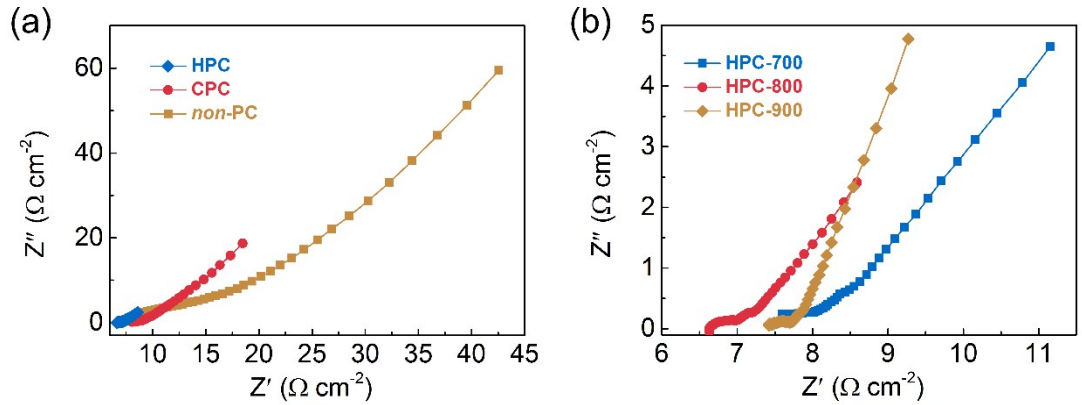

Figure S5. (a) Electrochemical impedance spectroscopy (EIS) of HPC, CPC and *non*-PC in 0.1 M KOH at 0.75 V *vs.* RHE with 5 mV AC potential from 100 kHz to 0.1 Hz. (b) Electrochemical impedance spectroscopy (EIS) of HPC-700, HPC-800 and HPC-900 in 0.1 M KOH at 0.75 V *vs.* RHE with 5 mV AC potential from 100 kHz to 0.1 Hz.

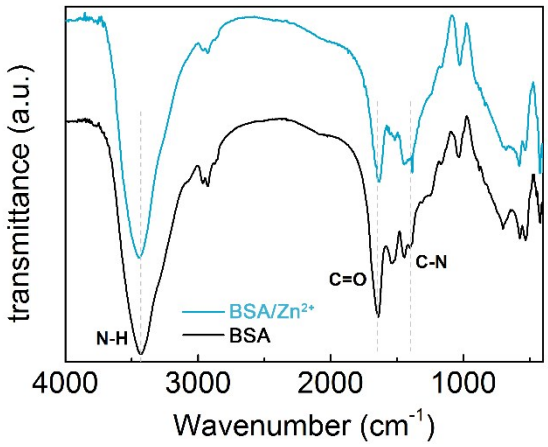

Figure S6. FT-IR spectrum of serum and BSA/$ZnCl_2$.

A conformation change of the BSA proteins appeared after the activating of disulfide bonds by Zn^{2+} under alkaline environment, which was demonstrated by the shift of N-H (from 3430 cm^{-1} to 3444 cm^{-1}), C=O (from 1646 cm^{-1} to 1635 cm^{-1}) and the weaken of C-N (1400 cm^{-1}).

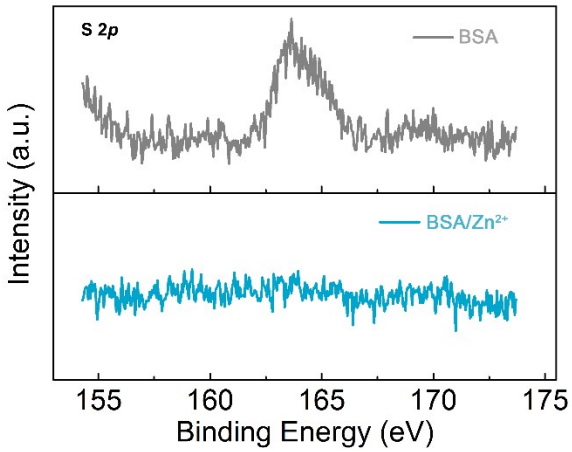

Figure S7. High-resolution XPS spectra of S 2p for BSA and BSA/Zn^{2+}.

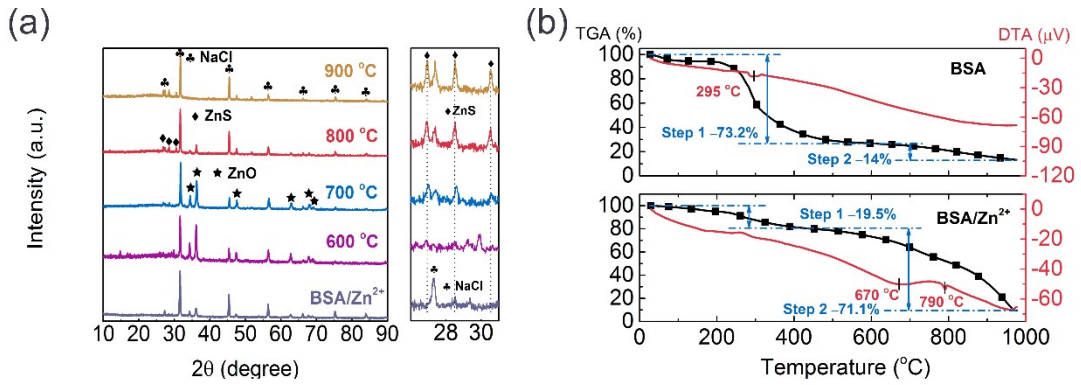

Figure S8. (a) XRD patterns of BSA/Zn^{2+} composite pyrolyzed at different temperatures. Right is the enlarged view of the XRD patterns in the range of 26-31°. (b) TG/DTA analysis of BSA and BSA/Zn^{2+} in Ar atmosphere.

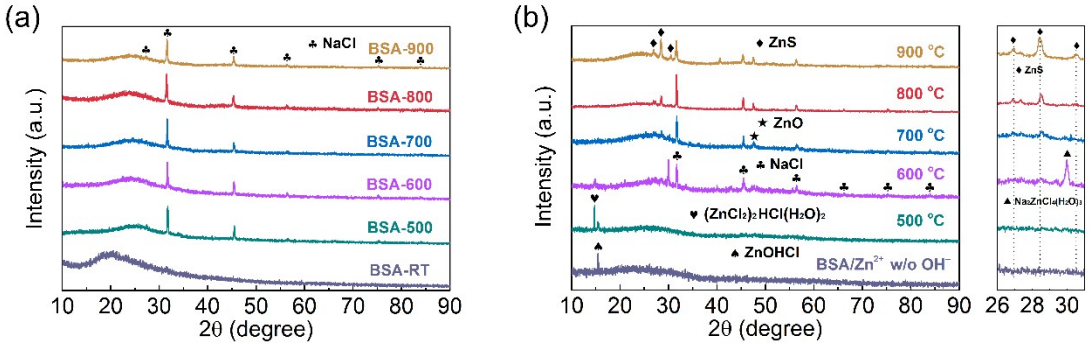

Figure S9. XRD patterns of (a) BSA and (b) BSA/Zn^{2+} without OH^- activation before pyrolysis and pyrolyzed at different temperatures. Right is enlarged view of the selected area in the XRD spectrum.

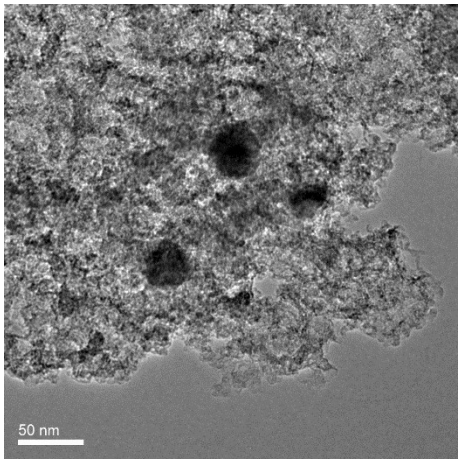

Figure S10. Typical TEM image of Fe-N-CPC.

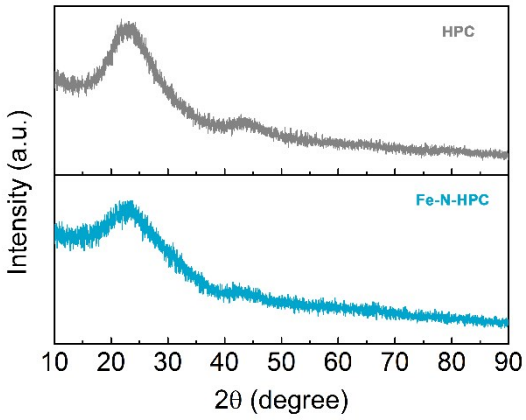

Figure S11. (a) XRD patterns of HPC and Fe-N-HPC.

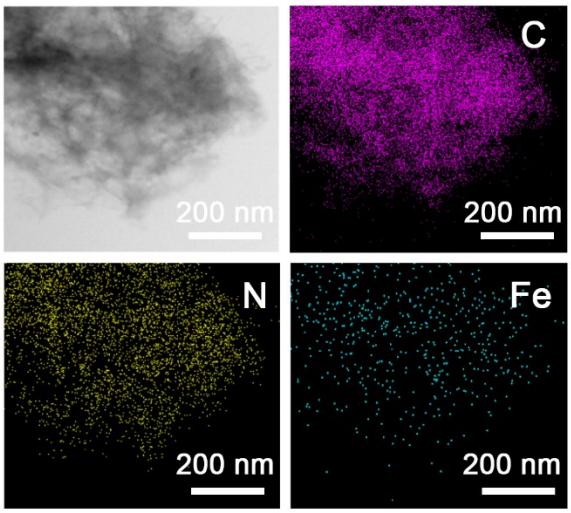

Figure S12. TEM and elemental mapping images of C, N, and Fe of Fe-N-HPC.

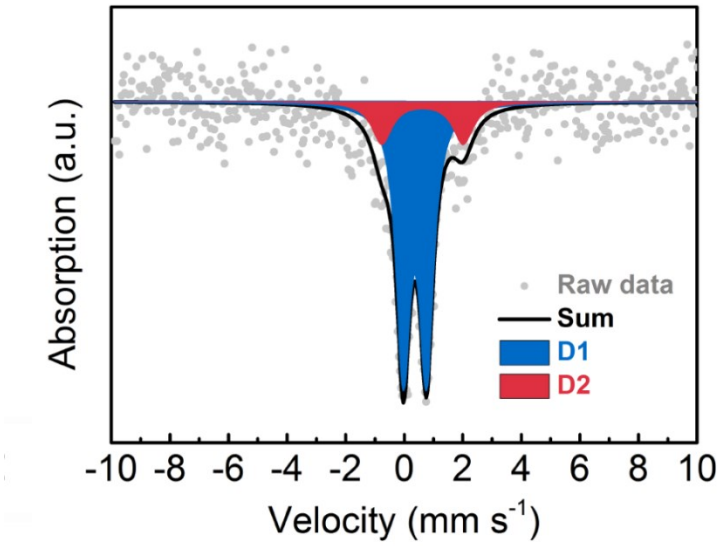

Figure S13. ^{57}Fe Mössbauer spectrum of Fe-N-HPC.

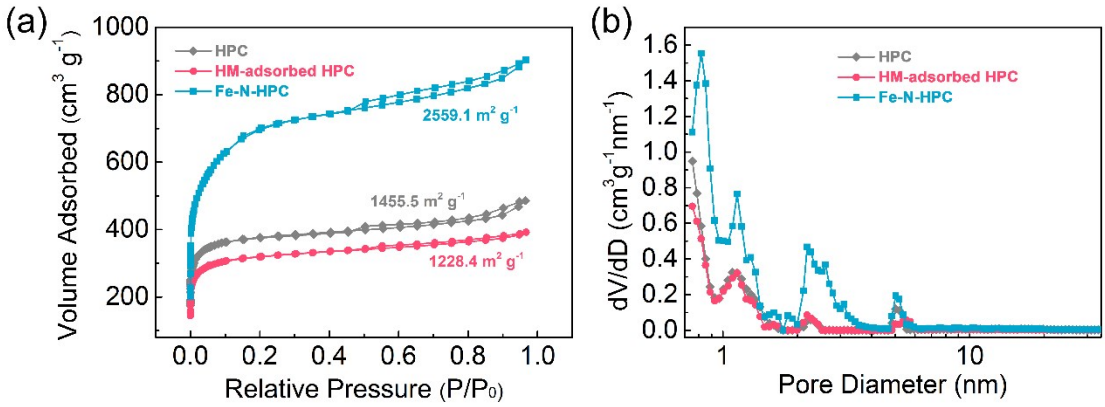

Figure S14. (a) Nitrogen adsorption-desorption isotherms and (b) corresponding DFT pore size distributions of HPC, HM-adsorbed HPC and Fe-N-HPC.

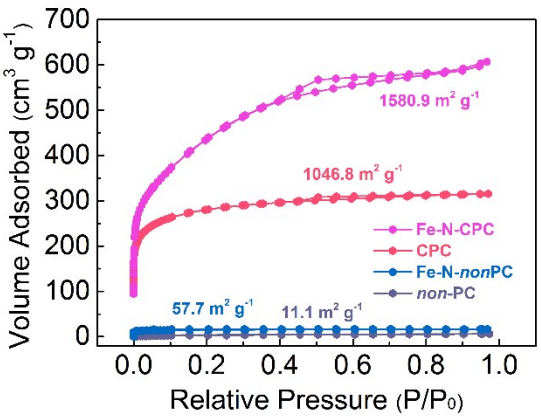

Figure S15. Nitrogen adsorption-desorption isotherms of *non*-PC, Fe-N-*non*PC, CPC and Fe-N-CPC.

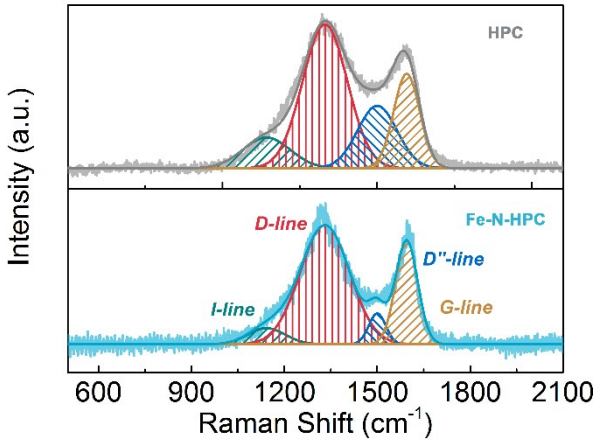

Figure S16. Raman spectra of HPC and Fe-N-HPC.

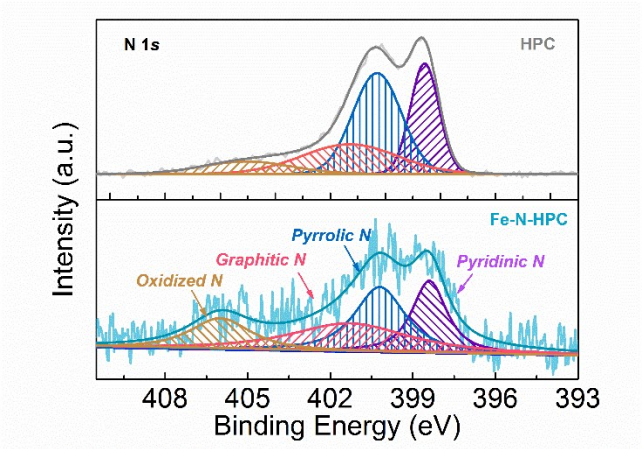

Figure S17. High-resolution XPS spectra of N 1s for HPC and Fe-N-HPC.

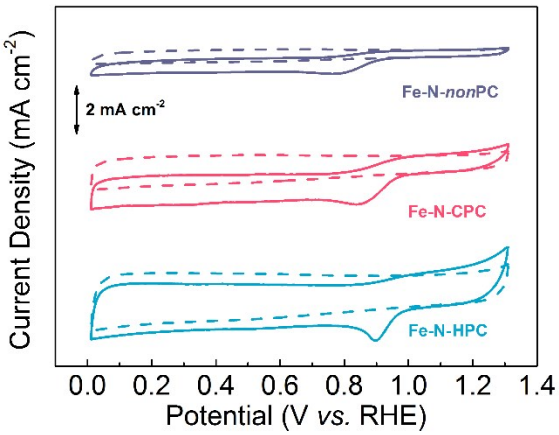

Figure S18. Cyclic voltammograms of Fe-N-*non*PC, Fe-N-CPC and Fe-N-HPC.

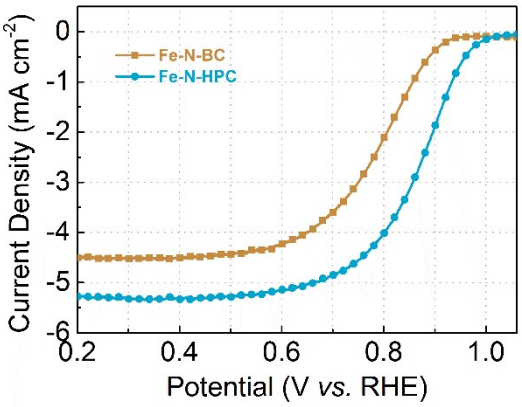

Figure S19. LSV curves of Fe-N-HPC and Fe-N-BC in O_2 saturated 0.1 M KOH at a sweep rate of 5 mV S^{-1} with a rotation rate of 1600 rpm.

The LSV measurement of Fe–N–BC was also conducted with an obviously inferior activity compared with the Fe-N-HPC, indicating the necessity of separation of red blood cells and serum albumin before the HPC and subsequent Fe-N-HPC preparation. The excellent activity of Fe-N-HPC can be attributed to high percentage of Fe–N_4 active sites and pronounced hierarchically porous structure.

REFERENCES

[1] J. Wang, H. Wu, D. Gao, S. Miao, G. Wang, X. Bao, *Nano Energy* **2015**, *13*, 387–396.

[2] G. A. Ferrero, K. Preuss, A. Marinovic, A. B. Jorge, N. Mansor, D. J. Brett, A. B. Fuertes, M. Sevilla, M.-M. Titirici, *ACS Nano* **2016**, *10*, 5922–5932.

[3] P. Chen, T. Zhou, L. Xing, K. Xu, Y. Tong, H. Xie, L. Zhang, W. Yan, W. Chu, C. Wu, Y. Xie, *Angew, Chem. Int. Ed.* **2017**, *56*, 610–614.

[4] A. Kong, C. Mao, Y. Wang, Q. Lin, X. Bu, P. Feng, *J. Mater. Chem. A* **2016**, *4*, 7305–7312.

[5] W. Zhang, X. Xu, C. Zhang, Z. Yu, Y. Zhou, Y. Tang, P. Wu, S. Guo, *Small Methods* **2017**, *1*, 1700167.

[6] J. Yang, X. Wang, B. Li, L. Ma, L. Shi, Y. Xiong, H. Xu, *Adv. Funct. Mater.* **2017**, *27*, 1606497.

[7] Q. Liu, X. Liu, L. Zheng, J. Shui, *Angew, Chem. Int. Ed.* **2018**, *57*, 1204–1208.

[8] F.-L. Meng, Z.-L. Wang, H.-X. Zhong, J. Wang, J.-M. Yan, X.-B. Zhang, *Adv. Mater.* **2016**, *28*, 7948–7955.

[9] Q. Lin, X. Bu, A. Kong, C. Mao, X. Zhao, F. Bu, P. Feng, *J. Am. Chem. Soc.* **2015**, *137*, 2235–2238.